Antiaromatic Covalent Organic Frameworks Based on Dibenzopentalenes

Josefine Sprachmann, Tommy Wachsmuth, Manik Bhosale, David Burmeister, Glen J. Smales, Zdravko Kochovski, Niklas Grabicki, Birgit Esser,* and Oliver Dumele*

Keywords: Covalent Organic Frameworks, Antiaromaticity, Non-alternant hydrocarbon, Dibenzopentalenes, Organic Batteries, Cathode active Materials, Photoconductivity

ABSTRACT: Despite their inherent instability, 4*n* π systems have recently received significant attention due to their unique optical and electronic properties. In dibenzopentalene, benzanellation stabilizes the highly antiaromatic pentalene core, without compromising its amphoteric redox behavior or small HOMO–LUMO energy gap. However, incorporating such molecules in organic devices as discrete small molecules or ill-defined amorphous polymers can limit the performance (e.g. due to solubility in the electrolyte solution or low internal surface area). Covalent organic frameworks, on the contrary, are highly ordered, porous, and crystalline materials that can provide a platform to align molecules with specific properties in a well-defined, ordered environment. We synthesized the first antiaromatic framework materials and obtained a series of three highly crystalline and porous covalent organic frameworks based on dibenzopentalene. Potential applications of such antiaromatic bulk materials were explored: COF films show a conductivity of 4×10^{-8} S cm^{-1} upon doping and exhibit photoconductivity upon irradiation with visible light. Investigations as battery electrode materials demonstrate their ambipolar nature and the ability to store both anions and Li ions with enhanced charge storage capabilities compared to an aromatic COF or the conductive carbon material. This work showcases antiaromaticity as a new design principle for functional framework materials.

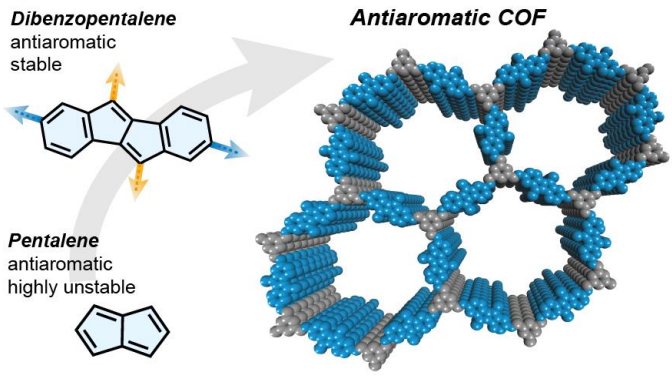

Introduction

In the field of organic materials, polycyclic aromatic molecules are receiving much attention owing to their electronic properties. According to Hückel's rule, aromatic molecules are planar systems with cyclic conjugated [4*n*+2] π-electrons resulting in substantial stabilization.

Contrarily, planar cyclic systems with 4*n* conjugated π-electrons experience destabilization and are termed antiaromatic.[1] Antiaromaticity comes with intriguing properties, such as a low HOMO–LUMO energy gap,[2] a low-lying triplet energy,[3–5] and redox activity.[6–10] However, utilizing these properties of is hampered by the inherent instability of such systems. Annellation of aromatic rings to (polycyclic) antiaromatic molecules[11–14] can drastically stabilize the reactive cores thermodynamically by adding local aromaticity to the system while retaining the peculiar properties ascribed to antiaromaticity.[9,15–19] For example, benzannellation to the highly antiaromatic unstable pentalene[20] leads to the benchtop-stable dibenzo[*a*,*e*]pentalene (DBP),[21–26] despite its 4*n* π-electron count (Figure 1a). DBP and related pentalene-based compounds show a low and tunable HOMO–LUMO energy gap[26] and a higher stability than acenes of similar size.[27] Thanks to these properties, we have seen a recent surge of interest in such polycyclic 4*n* π molecules for organic optoelectronics, such as organic field-effect transistors (OFETs)[7,28–30] or organic photovoltaics.[31–33] Another feature directly related to their antiaromatic nature is a reversible ambipolar redox behavior, unusual for pure hydrocarbons. When 4*n* π-systems are oxidized or reduced, the molecules experience aromatic stabilization in both the doubly-reduced and doubly-oxidized state resulting in a charged aromatic [4*n*+2] π-electron count.[34,35] Combined with their small HOMO–LUMO energy gap, this renders 4*n* π compounds potentially interesting candidates for functional materials.[22] However, applications of antiaromatic compounds as energy storage materials are rare.[8] One reason is that obtaining well-functioning battery electrodes from functional carbon-rich monomers remains a great challenge. Using discrete small molecules or ill-defined amorphous polymers in electrode-active materials can pose performance problems due to solubility in the electrolyte solution, instability in the charged state, or a low internal surface area for efficient ion diffusion.[36–38]

Some of these issues are addressed by covalent organic frameworks (COFs),[39,40] an emerging class of advanced materials. This class of well-defined porous materials can serve as a platform to translate the properties of molecules to bulk insoluble materials. The combination of a high surface area, accessible pores, and efficient electronic delocalization makes COFs ideal candidates for applications in energy storage,[41–43] as well as gas storage and separation,[44,45] (photo)catalysis,[46–49] and optoelectronics.[50–58] Analogous to crystalline COFs, amorphous porous organic polymers (POPs) are constructed of functional monomers. Although POPs lack the crystallinity of COFs, they are also valuable candidates for functional materials.[59–62]

The architecture of 2D COFs with their uniform channels, high stability and insolubility is especially ideal for applications as electrode-active material in batteries.[43,63–70] So far, mostly well-established organic redox units have been employed as active centers in COF-based

electrode-active materials.[71] Their redox activity is based on the presence of discrete redox centers, such as quinone groups, containing heteroatoms. On the other hand, antiaromatic molecules can consist solely of carbon and hydrogen atoms, but still show defined redox activity based on the aromatic stabilization of charged states. They have not yet been incorporated into COFs although such antiaromatic frameworks are an interesting target both as materials and from a fundamental perspective.[72] The ambipolar redox properties, together with the possibility of charge delocalization through close π–π stacking interactions in antiaromatic units,[73–75] hold potential for specific material properties.

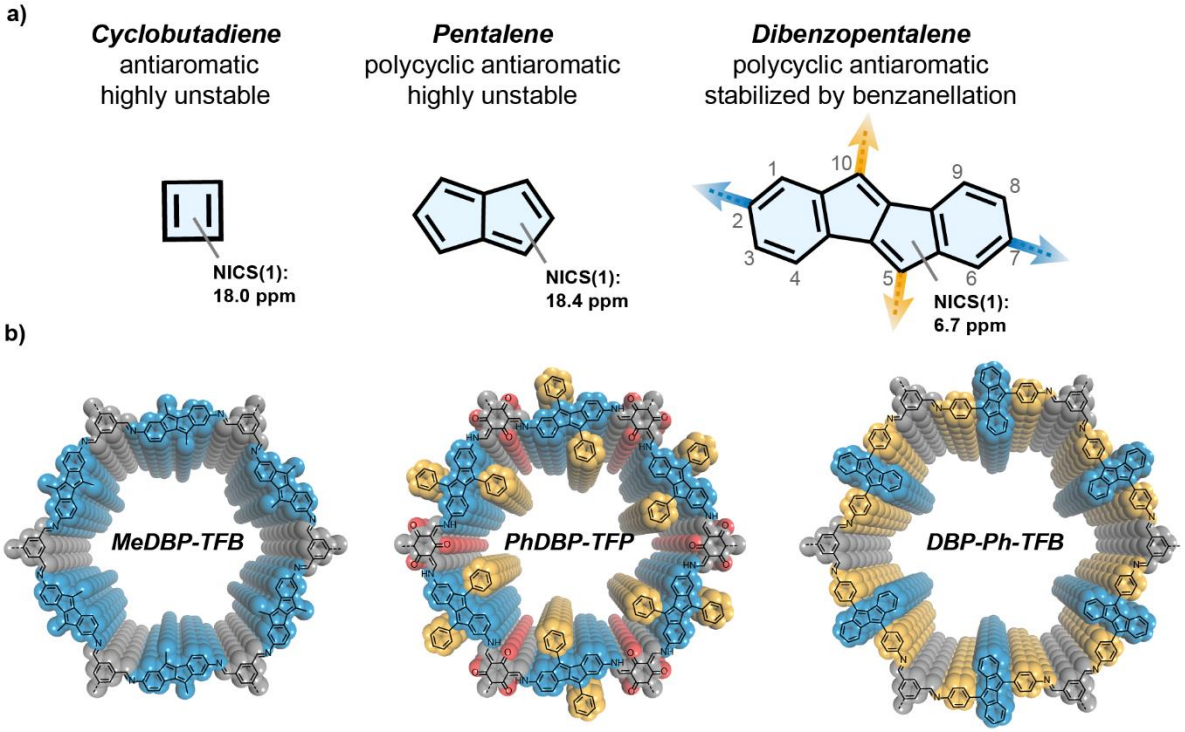

Figure 1. a) Structure of antiaromatic cyclobutadiene, pentalene, and dibenzo[*a*,*e*]pentalene with NICS(1) values (DFT, mPW1PW91/6-311+G(2d,p)) indicating an attenuated antiaromaticity in dibenzopentalene compared to pentalene; b) Structures of antiaromatic COFs presented in this work.

In this work, we designed a series of dibenzo[*a*,*e*]pentalenes and used them for the synthesis of imine-linked antiaromatic 2D COFs. We obtained three highly crystalline COFs and two amorphous POPs, all highly porous and stable materials based on DBP as 4*n* π building block. Antiaromatic COF films were used to explore the low optical band gap of such a material as a photoresponsive semiconductor with a conductivity of 4×10^{-8} S cm^{-1} after doping. We assembled battery cells with one of the antiaromatic DBP-COFs and one POP as electrode-active materials and investigated their charge storage properties as potential negative and positive electrode materials for Li-based batteries. Anion insertion occurs at high potentials of

ca. 3.9 V *vs*. Li/Li$^+$ with specific capacities of up to 30 mAh g^{-1}, while Li-ions insert at potentials around 0.5 V *vs*. Li/Li$^+$ and significant specific capacities of above 200 mAh g^{-1}. We show that the intrinsic ambipolar redox properties of the antiaromatic DBP units are transferred to the bulk materials for their application electrode materials as either negative or positive electrodes in rechargeable batteries.

Results and Discussion

Design and Synthesis of COF Building Blocks. We chose DBP as a COF building block for its ideal balance between stability and interesting properties based on its antiaromatic character. Nucleus-independent chemical shift (NICS)[76] values show a decreased antiaromaticity compared to the parent pentalene.[77–79] Polycyclic 4*n* π compounds with more pronounced antiaromatic character would hamper COF formation due to their limited thermal stability under the harsh reaction conditions used in reticular chemistry (typically 120 °C, 3 d). Despite their moderate antiaromaticity, DBP and its derivatives show remarkable redox properties and low, tunable band gaps, typical for 4*n* π systems.[16,26] We identified two possible linkage geometries — by a 2,7-substitution or 5,10-substitution — through which DBP can be incorporated into a COF as a (*pseudo*-)linear linker (Figure 1a).[80,81] To access imine-linked COFs, we installed benzophenone-protected amines at those positions. The benzophenone-imine groups serve a dual function: They are readily accessible via Buchwald–Hartwig imination reaction[82] from the corresponding bromides and are less prone to oxidation than the equivalent free diamines of DBPs that proved unstable in all our initial attempts. Additionally, benzophenone imines can be directly used in COF synthesis in place of amines improving the porosity of COFs compared to employing free amines.[83] In a formal transimination reaction an imine- or ketoenamine-connected COF is formed, and benzophenone is cleaved off.

For a 2,7-bisfunctionalized DBP, the Grignard addition of CH_3MgBr to dibromodiketone **1b**[77] promoted by $CeCl_3$ led to a diol that was subsequently dehydrated under acidic conditions affording the dimethyl-substituted DBP **2** in a yield of 67% (Scheme 1).[80] Buchwald–Hartwig imination of dibromide **2** using benzophenone imine as coupling partner gave dimethyl-bis(benzophenone imine) **3** in 90% yield. The same strategy was applied to achieve a different substituent at the 5,10-positions: The corresponding diphenyl-substituted COF linker **5** was synthesized analogously via dibromide **4**. To achieve a 5,10-linked DBP monomer, a different approach was necessary: For the synthesis of the 5,10-substituted DBP monomer **7**, a Li-organyl bearing the benzophenone imine unit was prepared from bromide **A**. The Li-organyl was reacted with diketone **1a**[77] to afford diol **6** in 68% yield. Dehydration of diol **6** without hydrolyzing the imine functionalities was achieved using Burgess's reagent as a selective, mild, non-acidic reagent yielding COF-linker **7** in 89%.[84] An attempted synthesis of **7** via Buchwald–Hartwig coupling of a 5,10-(4-bromophenyl)-DBP **S1** was not successful as the

reaction led to an inseparable mixture (debromination products among others). To our surprise, 5,10-linked bis(benzophenone imine) **7** is hardly soluble in common organic solvents making even ^{1}H-NMR spectroscopy challenging. This is unusual as its 5,10-bromophenyl-substituted analogue **S1** is sufficiently soluble, and typically benzophenone imine substitution enhances solubility.[83]

Scheme 1. Synthesis of DBP-based COF building blocks[a]

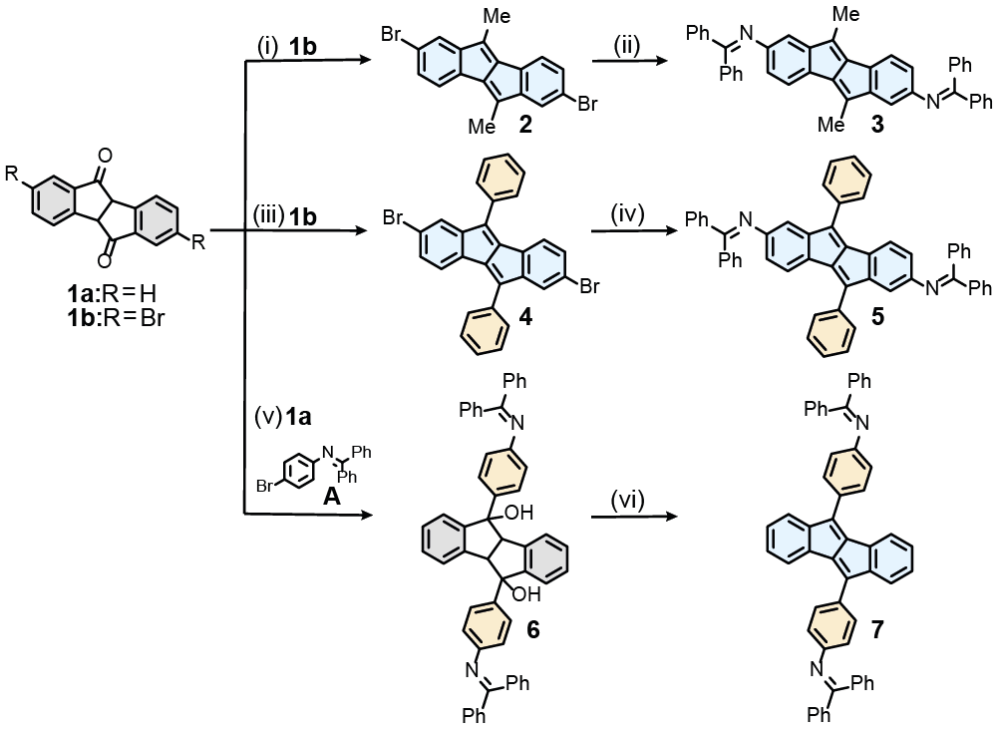

[a]Reagents and conditions: (i) 1) $CeCl_3$, CH_3MgBr, **1b**, 0→25 °C, 4 h; 2) *p*TsOH, toluene, 110 °C, 4 h, 67%; (ii) $Pd(dba)_2$, BINAP (*rac*), NaO*t*Bu, benzophenone imine, 100 °C, 2 h, 90%; (iii) 1) $CeCl_3$, PhMgBr, **1b**, 0→25 °C, 20 min; 2) *p*TsOH, toluene, 110 °C, 4 h, 54%; (iv) $Pd(dba)_2$, BINAP (*rac*), NaO*t*Bu, benzophenone imine, 100 °C, 1 h, 79%; (v) **A**, *n*BuLi, then **1a**, THF, –78→25 °C, 3 h, 68%; (vi) Burgess reagent, toluene, 110 °C, 1 h, 89%.

The optical, electrochemical, and structural properties of DBPs **2**–**7** were consistent with previous reports of DBPs.[16,26,28,77,78] The UV-vis spectra are typical for DBPs with their lowest energy transition being symmetry-forbidden (HOMO→LUMO).[15] The spectra of the DBP **3**, **5**, and **7** imines show a bathochromic shift compared to the respective DBP bromides **2**, **4**, and **S5**. Cyclic voltammetry shows the amphoteric redox behavior of the DBPs (SI, Section S14). The DBPs **2** and **3** with methyl groups in the 5,10-positions show irreversible reduction and oxidation waves, while 5-10-phenyl substitution (in **4** and **5**) leads to an improved (pseudo)-reversible reduction and oxidation. The antiaromatic character of the target compounds is reflected in their nuclear magnetic resonance (NMR) spectra: In line with reported DBPs, the ^{1}H NMR signals of the benzenic protons at the DBP appear upfield shifted (6.15–7.14 ppm)

relative to ^{1}H NMR signals of fully aromatic molecules (naphthalene:7.47–7.84 ppm). NICS(1) calculations (level of theory: DFT:mPW1PW91/6-311G+(2d,p)) reveal paratropicity in the 5-membered rings and diatropicity in the 6-membered rings, analogous to reported DBP derivatives[77] (e.g. for **5**: $NICS(1)_{5\text{-ring}}$ = 6.26 ppm, $NICS(1)_{6\text{-ring}}$ = –4.61 ppm, see SI, Section S16). Single-crystals suitable for X-ray crystallography were grown for DBPs **2**, **4**, and **7**. They show bond length alternations typical for compounds with antiaromatic character and a herringbone packing typical for DBPs (SI, Section S15).

COF Synthesis and Characterization. For COF construction, we reacted the three DBP-based linear linkers **3**,**5**, and **7** with the commercially available triformylbenzene (**TFB**), forming an imine bond, or with trihydroxytriphloroglucinol (**TFP**), forming a keto-enamine by keto–enol-tautomerization after imine bond formation. After solvothermal synthesis, we obtained three crystalline porous COFs and two amorphous porous polymers (POPs, Figure 2).

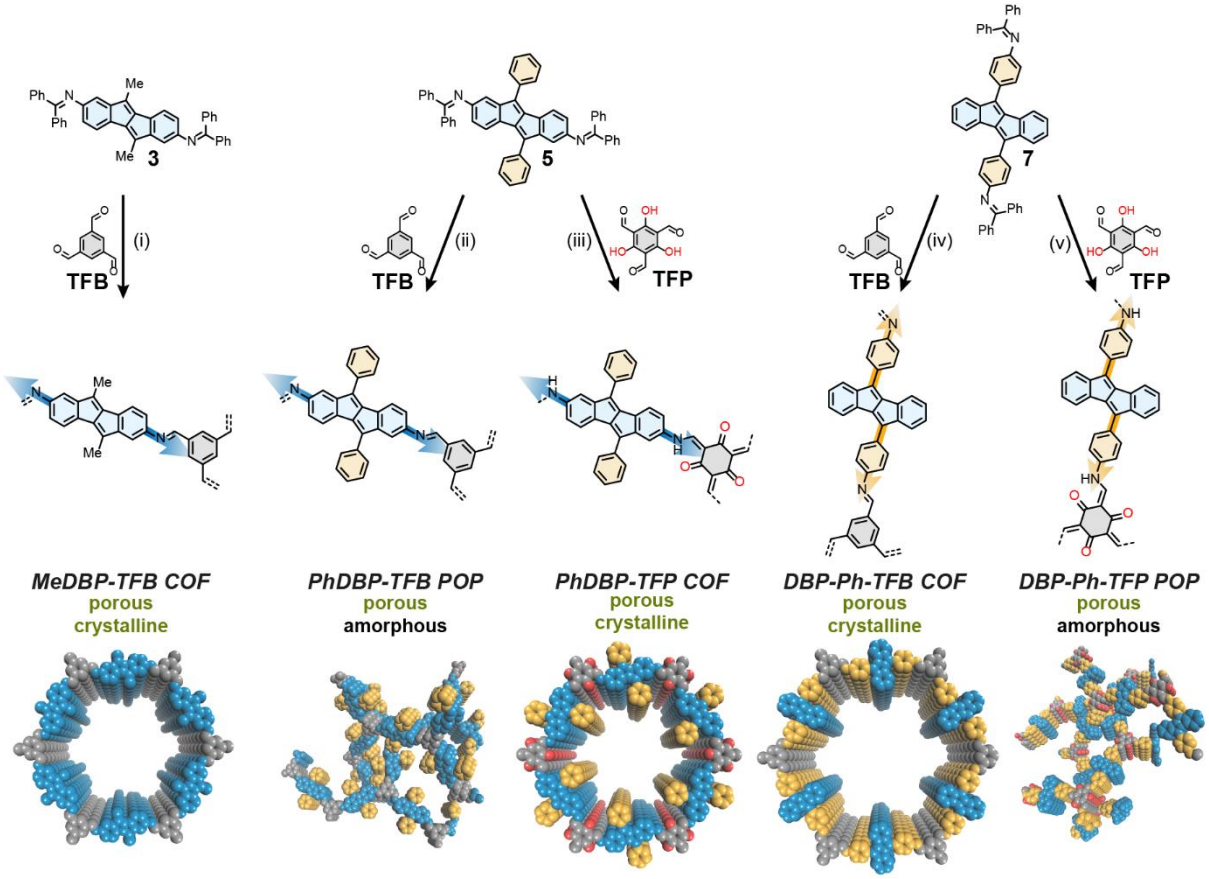

Figure 2. Construction of DBP-based COFs and POPs from linearly functionalized DBPs **3**, **5**, **7** with trigonal nodes **TFB** and **TFP**. Reagents and conditions (i–v): acid, mesitylene/1,4-dioxane 1:1, 120 °C, 3 d, with the following specifications: (i) aq. acetic acid (6 M, 18 equiv.), 88%; (ii) aq. TFA (6 M, 18 equiv.), 92%; (iii) aq. TFA (6 M, 18 equiv.), 77%; (iv) trifluoromethanesulfonic acid (conc., 6 equiv.), 71%; v) acetic acid (6 M, 6 equiv.), 76%

MeDBP-TFB COF was synthesized under solvothermal conditions (mesitylene/1,4-dioxane 1:1, 6 equiv. trifluoromethanesulfonic acid (TFA), 120 °C, 3 d). Powder X-ray diffraction (PXRD) showed narrow reflexes revealing structural features and confirming the formation of a highly crystalline framework (Figure 3b). Comparison with a simulated diffraction pattern from structural model using Materials Studio program package[85] showed agreement with an eclipsed AA stacking pattern. Pawley refinement in the hexagonal *P*6/*m* space group provided a good fit in agreement with the experimental data (refined lattice parameters $a = b = 32.5$ Å and $c = 3.8$ Å). The most intense reflex was observed at $2\theta = 3.3°$ corresponding to the (100) Bragg reflection as well as a reflex at 6.5° corresponding to the (200) plane. The planes (110) and (120) are represented in more weakly resolved reflexes at 5.7° and 8.7°, respectively. A broad reflex was observed at 25.8° corresponding to the (001) plane and confirming the π–π stacked 2D-structure at a layer-distance of 3.8 Å. Nitrogen (N_2) adsorption–desorption measurements at 77 K confirmed permanent porosity of **MeDBP-TFB** COF (Figure 3c). A steep initial increase in $p/p_0 = 0$ to 0.02 suggests a type I isotherm, confirming microporosity of the framework.[86] The surface area was calculated using the Brunnauer–Emmet–Teller (BET) method, showing high porosity with 790 $m^2\ g^{-1}$. The pore size distribution within the material was calculated from the adsorption isotherm using nonlinear density functional theory (NL-DFT), showing a narrow distribution of pore sizes centered at around 25 Å (Figure 3c, inset). Examination of the morphology using scanning electron microscopy (SEM) revealed highly uniform aggregates of spherical particles of ~1 µm diameter (Figure 4 a,b). Fourier-transform infrared spectroscopy (FT-IR) and cross-polarization magic-angle spinning nuclear magnetic resonance (CP-MAS NMR) were used to examine the chemical composition of **MeDBP-TFB** COF (SI, Figures S26, S31). Complete formation of the imine bond was confirmed by the absence of the C=O stretch of **TFB** at 1695 cm^{-1}, while the C=N imine stretch was detected at 1595 cm^{-1}. The CP-MAS NMR spectrum showed a peak at 9.5 ppm corresponding to the CH_3-group, along with overlapping peaks from 120–153 ppm corresponding to the aromatic carbons and the imine carbon, as expected in the same area. The absence of an aldehyde signal around 200 ppm again indicated full conversion of the monomers.

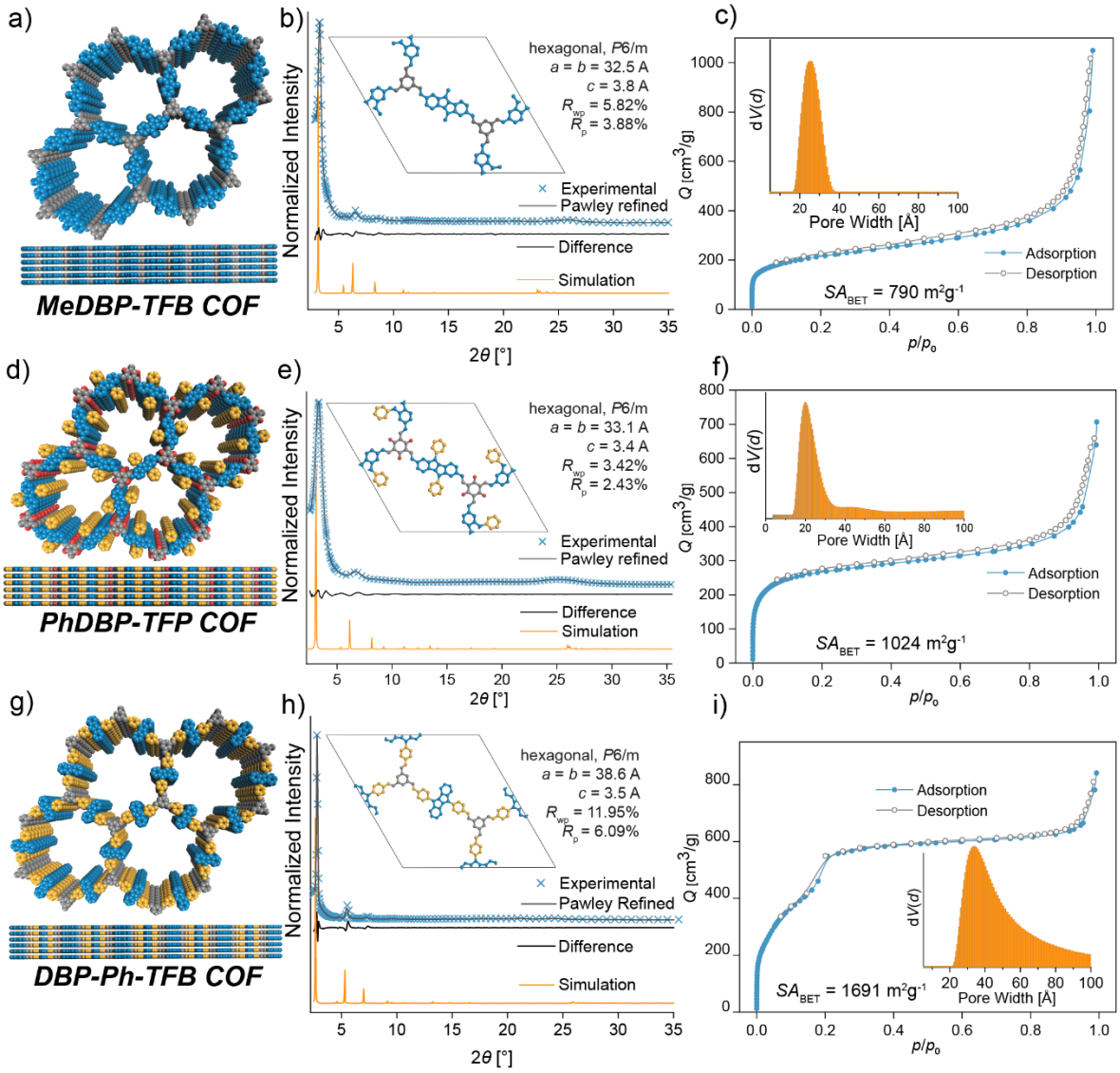

Figure 3. Characterization of DBP COFs. a,d,g) Structural model of **MeDBP-TFB** COF, **PhDBP-TFP** COF, **DBP-Ph-TFB** COF; b,e,h) PXRD data of **MeDBP-TFB** COF, **PhDBP-TFP** COF, and **DBP-Ph-TFB** COF: experimental PXRD pattern (blue crosses), Pawley refinement (grey line) using an optimized structural model (inset), difference between Pawley refinement and experimental data (black line), simulated PXRD pattern (orange); c,f,i) N_2 sorption isotherms of **MeDBP-TFB** COF, **PhDBP-TFP** COF, and **DBP-Ph-TFB** COF: N_2 adsorption isotherm (blue), N_2-desorption isotherm (grey), inset: pore size distribution simulated by NL-DFT based on sorption data.

Attempts to reticulate phenyl-substituted DBP **5** with **TFB** to a COF (mesitylene/1,4-dioxane 1:1, 18 equiv. TFA) resulted in a non-crystalline porous polymer **PhDBP-TFB** POP. Even though the material showed high porosity with a BET surface area of 669 $m^2\ g^{-1}$, it proved to be fully amorphous in PXRD analysis (SI, Figures S3, S4, S19). In an extensive screening of the solvent system, monomer concentration, type of acid, and amounts of acid, no crystalline COFs but only amorphous porous polymers were produced. Despite its lack of crystallinity, the material showed a narrow pore size distribution calculated from the N_2-adsorption isotherm by NL-DFT, a uniform particle size under SEM, and narrow signals in CP-MAS NMR spectroscopy (SI, Figures S12, S27, S42). To extend our screening, we replaced **TFB** by

triformylphloroglucinol (**TFP**) as a node. Using **TFP**, the newly formed imine linkage is transformed to a β-ketoenamine by irreversible keto–enol tautomerization, often leading to improved stability compared to COFs containing the **TFB** node.[87] To our delight, the reaction of DBP **5** and **TFP** (mesitylene/1,4-dioxane 1:1, 28 equiv. TFA) yielded crystalline **PhDBP-TFP** COF as confirmed by PXRD (Figure 3e). The experimental data matched well with the X-ray diffraction pattern calculated from an AA-stacked model. Pawley refinement in the *P*6/*m* space group provided a good fit with the experimental data, yielding refined lattice parameters of $a = b = 33.1$ Å and $c = 3.4$ Å. The reflex corresponding to the (100) plane was observed as the most intense signal at 3.3°, as well as the (200) and (001) reflex at 6.7° and 25.3°, respectively. N_2-sorption showed a type I isotherm and BET analysis revealed a high internal surface area of 1024 $m^2\ g^{-1}$ (Figure 3f). Using NL-DFT, a narrow pore size distribution centered around 20 Å was derived from the adsorption isotherm (Figure 3f inset). Low-dose high-resolution transmission electron microscopy (HR-TEM) revealed uniform rod-shaped crystallites and consistent lattice fringes with 1.24 nm spacing corresponding to the (200) reflex, indicative of the crystalline nature of the material (Figure 4c, Section S9). The CP-MAS NMR spectrum showed a peak at 184.0 ppm, corresponding to the ketone-carbon, next to an overlapping set of signals from 100–150 ppm corresponding to the aromatic and enamine carbons (SI, Figure 28). FT-IR shows the characteristic C=O stretch at 1573 cm^{-1}, confirming the ketoenamine form of the linkage (SI, Figure S33).

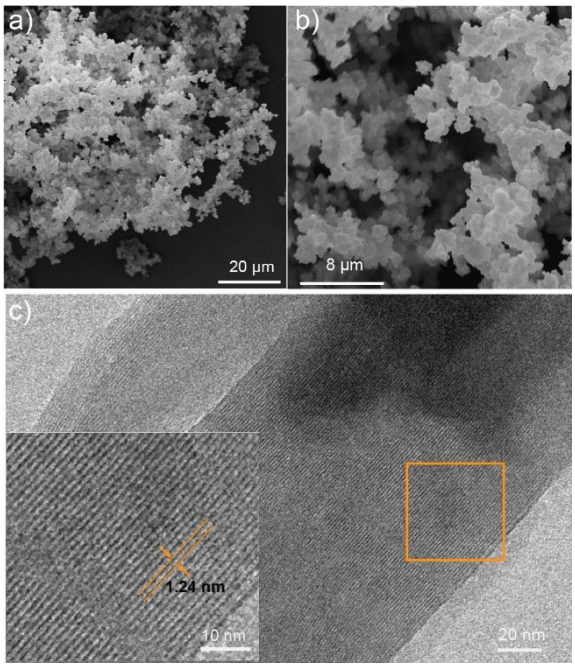

Figure 4. a,b) SEM image of **MeDBP-TFB** COF bulk powder sample showing uniform particles; See the Supporting Information for analogous images of all other COFs and POPs. (SI, Section S10). c) Low-dose HR-TEM image of a **PhDBP-TFP** COF crystallite (~500 × 130 nm) featuring lattice fringes with 1.24 nm distance corresponding to the (200) reflex; inset: zoom-in.

Using DBP as a COF linker through its 5- and 10-position, DBP **7** was reacted with **TFB** and **TFP**, respectively. Here, to our surprise, only the condensation with the **TFB** node yielded crystalline **DBP-Ph-TFB** COF, while reticulating the same monomer **7** with **TFP** yielded amorphous **DBP-Ph-TFP** POP, in contrast to our findings with DBP linker **5**. The **DBP-Ph-TFB** COF was synthesized in mesitylene/1,4-dioxane 1:1 using six equivalents of trifluoromethanesulfonic acid. PXRD shows narrow reflexes at 2.8°, 4.8°, 5.5°, and 7.3°, corresponding to the (100), (110), (200), and (120) planes, respectively (Figure 3h). The experimental data agrees with the diffraction pattern of an AA-stacked model and Pawley refinement in the *P*6/*m* space group gave lattice parameters of $a = b = 38.6$ Å and $c = 3.5$ Å. The N_2-sorption isotherms show a clear step around $p/p_0 = 0.2$, indicating a Type IV isotherm and mesoporosity in accordance with the expected pore size, larger than **MeDBP-TFB** COF and **PhDBP-TFP** COF (Figure 3i). In contrast, non-crystalline **DBP-Ph-TFP** POP does not show a step around $p/p_0 = 0.2$, typical for a type IV isotherm, likely indicating an overall lower degree of order (SI, Figure S9). The materials exhibit a BET-surface area of 1691 $m^2\ g^{-1}$ and 497 $m^2\ g^{-1}$ for **DBP-Ph-TFB** COF and **DBP-Ph-TFP** POP, respectively. The pore size distribution calculated by NL-DFT from the adsorption isotherm shows a narrow range around 38 Å (Figure 3i inset).

Optical and Electronic Properties. The optical properties of the antiaromatic COFs and POPs were studied using diffuse reflectance UV-vis spectroscopy. The spectra of the powders revealed broad absorptions with onsets in the visible range beyond 700 nm (Figure 5). **PhDBP-TFP** COF shows the most red-shifted absorption onset. The optical band gaps were determined by Tauc plots and range from 1.3 eV to 1.7 eV with **PhDBP-TFP** COF having the smallest band gap. The trends observed in the diffuse reflectance UV-vis spectra matched with UV-vis spectra of COF dispersions, with **PhDBP-TFP** COF having the most red-shifted absorption maximum.

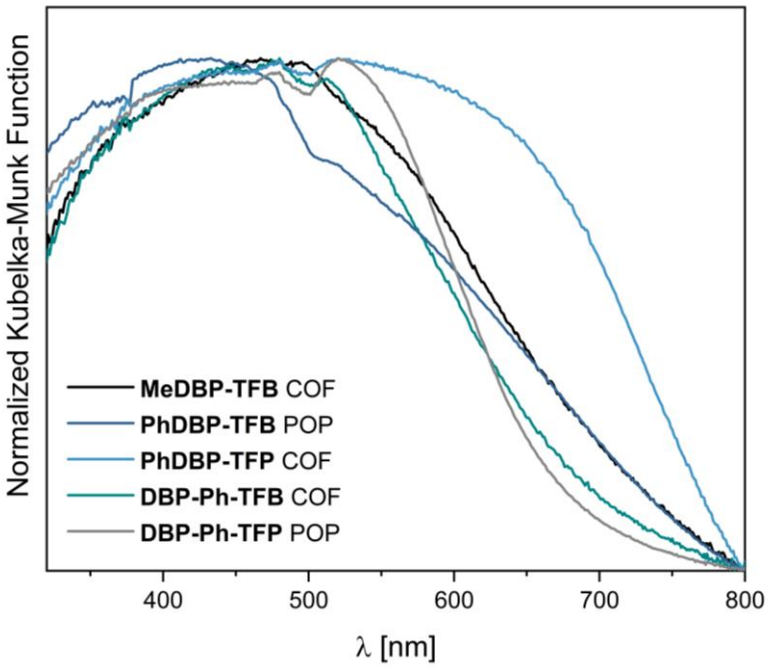

Figure 5. Normalized diffuse reflectance UV-vis spectra of synthesized COF and POP powders.

To investigate the intrinsic conductivity of the material, we fabricated COF thin films. **PhDBP-TFP** COF was chosen for its smallest optical band gap of this series and dispersions were produced by acid-mediated exfoliation.[88] The dispersion was dropcast onto an interdigitated indium tin oxide (ITO) substrate. Alternatively, acid-free exfoliation by ultrasonication and subsequent dropcasting yielded similar results. Both films were dried under vacuum. Applying a voltage bias of 20 V, the COF showed a low conductivity of 1×10^{-12} S cm^{-1}. p-Type doping by exposure to I_2 vapor (15 h, room temperature) increased the conductivity by four orders of magnitude to 4×10^{-8} S cm^{-1} (Figure 6 a,b). Upon irradiation with UV or visible light, the films show photoconductivity. While irradiating with 375 nm, 405 nm, 505 nm, or 660 nm the conductivity approximately doubled (Figure 6a). Even after 100 on/off cycles (10 s on, 10 s off) the material showed no signs of fatigue (Figure 6c). The **PhDBP-TFP** COF films showed an equal on/off ratio in photoresponsive conductivity in the doped and undoped state. Overall, the conductivity is most likely limited not by properties native to DBP-COFs but by the poor film quality. A heterogeneous film morphology and grain boundaries hamper the efficient charge transport. Similarly, the slow response time/long carrier lifetime is likely a feature of the material quality and not an intrinsic property of the DBP functionalities. Processing as well as growing COFs into homogeneous highly crystalline thin film remains a challenge and improving the film quality will be necessary to harness the full potential of our materials. Hence, we further investigated energy storage application using the bulk COF materials.

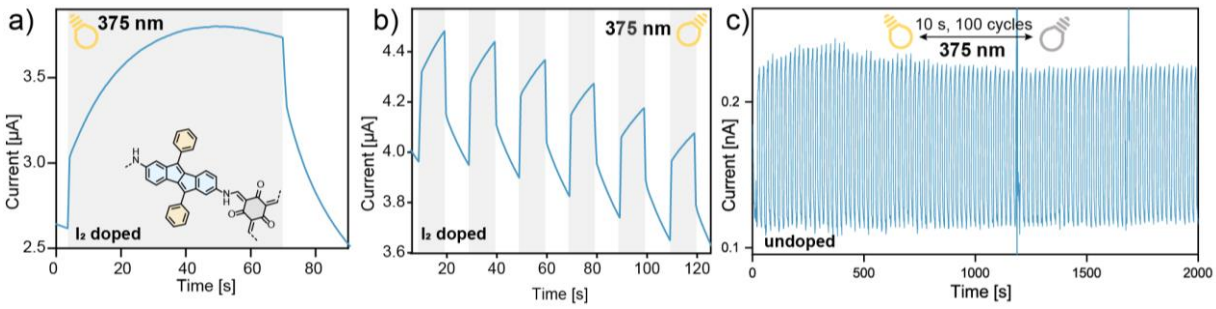

Figure 6. a) Conductivity of an I_2-doped **PhDBP-TFP** COF film at 20 V bias under irradiation with a 375 nm LED (grey background); b) conductivity of I_2-doped **PhDBP-TFP** COF film at 20 V bias with 10 s irradiation pulses by a 375 nm LED (grey shaded); c) conductivity of **PhDBP-TFP** COF film at 20 V bias with 10 s irradiation pulses by a 375 nm LED over 100 cycles.

Energy Storage Properties.

The interplay between aromatic and antiaromatic states can enable a defined redox activity in carbon-rich materials, which is usually only be observed for compounds containing heteroatoms and localized redox-active groups. For DBP derivatives, this is manifested in ambipolar electrochemical behavior and both accessible oxidation and reduction events,[26,35] which, however, has not been explored in charge storage applications. Few other examples exist, such as an antiaromatic norcorrole used as battery electrode material[8] or a purely hydrocarbon paracyclophane-1,9,17,25-tetraene,[89] switching from local to global aromaticity upon reduction. To evaluate the energy storage capabilities of the antiaromatic DBP-COFs, their electrochemical properties were investigated in dual-ion and cation-rocking chair Li-organic batteries. Of all DBP materials reported herein, the 2,7-linked **PhDBP-TFP** COF and the 5,10-connected **DBP-Ph-TFP** POP gave the best results, which will be discussed in the following. Composite electrodes consisting of 30 wt% COF or POP, 50 wt% acetylene black as conductive carbon additive and 20 wt% PVdF binder on Al or Cu foil were investigated in coin cells *vs*. Li as counter electrode, using 1 M $LiPF_6$ in EC/DMC 1:1 as electrolyte.

As positive electrode materials in a dual-ion Li-organic battery, the cyclic voltammograms (CVs) in the potential range of 3.0–4.2 V *vs*. Li/Li^+ showed a redox event above 3.8 V with a peak potential at ca. 4.0 V (noticeable for the **PhDBP-TFP** COF, Figure 7a). This redox potential corresponds well to the oxidation of the DBP core, as a comparison with compound **3** (Figure S62, anodic peak potential = 0.55 V *vs*. Fc/Fc^+) and compound **5** (Figure S64, 0.75 V *vs*. Fc/Fc^+) shows (assuming 3.25 V for Fc/Fc^+ *vs.* Li/Li^+ [90]). Cycling to higher cut-off voltages of up to 4.4 V led to irreversible side reactions, which can occur with the electrolyte. In the CV, **PhDBP-TFP** COF shows a higher integral charge area compared to **DBP-Ph-TFP** POP, which is also reflected in the galvanostatic cycling experiments. As the charge/discharge curves of the second cycles at 100 mA g^{-1} current density show, with 26 mAh g^{-1} the specific discharge

capacity of **PhDBP-TFP** COF is much higher than that of **DBP-Ph-TFP** POP with 14 mAh g^{-1} (Figure 7b). These values correspond to 47% respective 25% of the theoretical specific capacities of the COFs, amounting to 54.8 mAh g^{-1} for both **PhDBP-TFP** COF and **DBP-Ph-TFP** POP, assuming a one-electron oxidation. In both cases, a plateau centered around 3.95 V *vs*. Li/Li^+ is visible, a high value for COFs,[64,91,92] at which anion insertion occurs here concurrent with the oxidation of the DBP-COF. The electrochemical performance of acetylene black was also measured, contributing only 2 mAh g^{-1} in the same potential range to the electrode performance (SI, Figure S70)). Both **PhDBP-TFP** COF and **DBP-Ph-TFP** POP show a good rate performance with only small capacity losses when increasing the C-rate from 0.4 to 10 C, and even rates as high as 20 C and 40 C resulted in significant measurable specific capacities (Figure 7c). Decreasing the C-rates to 0.4 C refurbished the initial specific capacities, demonstrating that no decomposition of the active material took place.

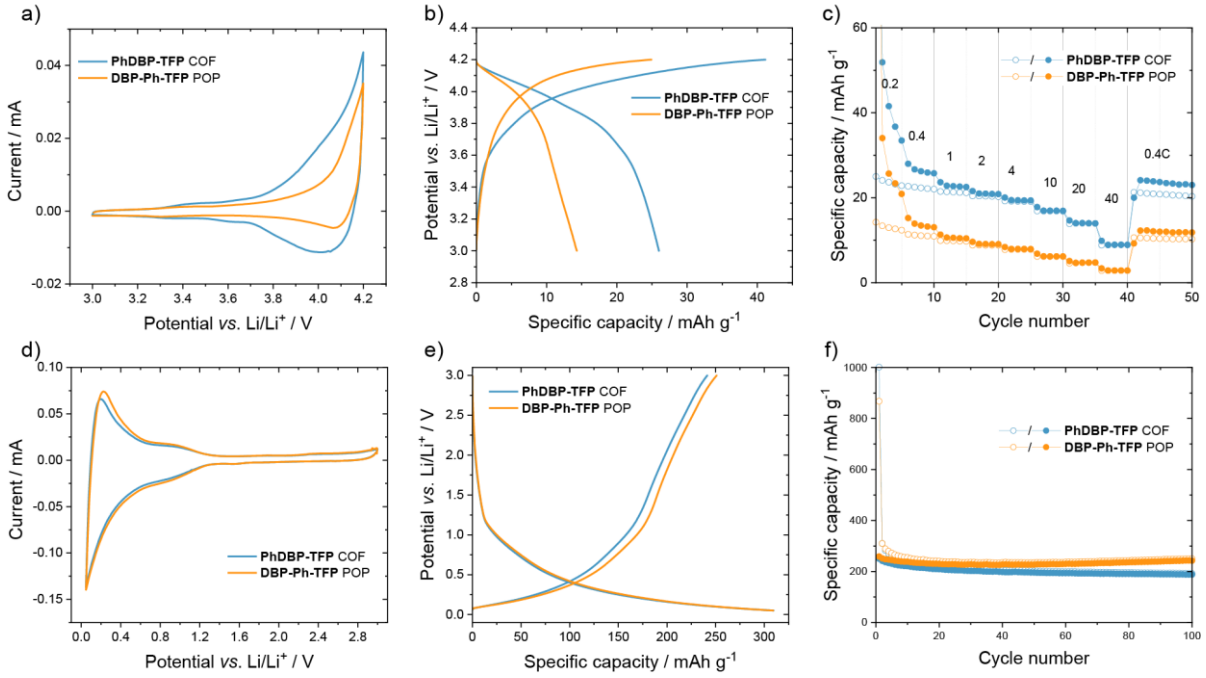

Figure 7. Electrochemical performance of **PhDBP-TFP** COF and **DBP-Ph-TFP** POP in composite electrodes (COF or POP/acetylene black/PVdF binder (30:50:20 wt%), 1 M $LiPF_6$ in EC/DMC (1:1), counter electrode: Li foil, a)–c) as positive electrode materials on Al foil, d)–f) as negative electrode materials on Cu foil). a, d) Cyclic voltammograms (2^{nd} cycle, 0.2 mV s^{-1}); b, e) Charge/discharge curves during constant current cycling at 100 mA g^{-1}, 2^{nd} cycle; c) Rate performance; f) Cycling performance at 100 mA g^{-1} (solid symbols represent the charge capacity, and open symbols represent the discharge capacity).

The anion storage in the DBP COFs can occur either through localized redox reactions at the DBP units as redox-active sites, or as storage of anions in the COF framework, in which case the charges would be more distributed over the COF. To evaluate the storage mechanism, we investigated 5,10-diphenyl-DBP as small molecule DBP derivative as well as the aromatic **BND-TFP** COF (in some reports referred to as **TpBd** COF[93]). **BND-TFP** COF is structurally analogous to **PhDBP-TFP** COF, but the DBP units are replaced by biphenyl groups, which

lack antiaromaticity (structures in SI, Figure S69). Both 5,10-diphenyl-DBP[81] and **BND-TFP** COF[83] were synthesized according to the literature. The 5,10-diphenyl-DBP electrodes showed clear redox events in the CVs with an anodic peak potential of 4.08 V and a cathodic peak potential of 3.72 V vs. Li/Li^+ (SI, Figure S71) with a distinctly different signature than the CVs of the DBP-COFs in **Figure 7**a. Constant current cycling measurements resulted in a specific discharge capacity of 31 mAh g^{-1}, which decreased to 22 mAh g^{-1} over 50 cycles due to dissolution of the small molecule in the electrolyte. Compared to the theoretical specific capacity of 5,10-diphenyl-DBP of 75.6 mAh g^{-1} (for a one-electron oxidation), these values are low, and likely also related to dissolution. The **BND-TFP** COF-electrodes, on the other hand, gave CV profiles resembling those of **PhDBP-TFP** COF (SI, Figure S72), indicating a similar charge storage mechanism occurring in both materials. However, the available specific discharge capacities for **PhDBP-TFP** COF were higher than for **BND-TFP** COF, which in the second cycle afforded a value of only 19 mAh g^{-1}. Hence, even though the redox reactions do not seem to be entirely centered on the (antiaromatic) DBP units, the DBPs enhance the charge storage capabilities of the COF when compared to biphenyl units significantly.

Investigating **PhDBP-TFP** COF and **DBP-Ph-TFP** POP as negative electrode materials in a Li-ion-rocking chair configuration, the CVs in the potential range of 3.0–0.05 V *vs*. Li/Li^+ showed a peak in cathodic scan direction with a peak potential of ca. 1.0 V, a sharp current increase towards 0.05 V, and two peak potentials in cathodic scan direction at ca. 0.3 and 1.0 V in the second cycle (Figure 7d). In the first cycle, both materials showed irreversible peaks in cathodic scan direction at 1.66 and 0.64 V *vs*. Li/Li^+, the latter related to the formation of a solid–electrolyte interphase.[94] The charge/discharge curves from constant current cycling measurements confirm that the Li-ion intercalation occurs between 0.05–1.2 V and furnishes specific capacities of 309 mAh g^{-1} for the second cycle for both materials (Figure 7e). Cycling at 100 mA g^{-1} for 100 cycles interestingly showed a higher cycling stability for the **DBP-Ph-TFP** POP than for the **PhDBP-TFP** COF with a capacity retention of 80% *vs*. 62%, respectively (Figure 7f). Since the reduction of the DBP unit is expected to occur at ca. 1.6 V *vs*. Li/Li^+ (based on the reported reduction potential of 1,5-diphenyl-DBP of −1.68 V *vs*. Fc/Fc^+[95] and assuming 3.25 V for Fc/Fc^+ *vs.* Li/Li^+ [90]), the electrochemical signature of the DBP-COF/POP resembles more that of carbon materials. Indeed, electrodes only consisting of acetylene black (and binder) showed a CV profile similar to those in **Figure 7**d (SI, Figure S73). However, the specific capacities were higher with **PhDBP-TFP** COF and **DBP-Ph-TFP** POP than those with acetylene black alone (177 mAh g^{-1} for the second cycle). An almost identical electrochemical behavior was measured for **BND-TFP** COF with a specific discharge capacity of 255 mAh g^{-1} for the second cycle (SI, Figure S74), indicating that the reason of the advanced Li-ion storage in the COFs compared to acetylene black is related to their ordered and porous structure rather than the presence of (antiaromatic) redox-active centers.

In summary, the antiaromatic **PhDBP-TFP** COF and **DBP-Ph-TFP** POP showed electrochemical activity both as positive and negative electrode materials. Compared to a similar but aromatic COF, anion storage in the high voltage range occurred with higher specific capacities, while in the negative potential range the COFs improved the Li-ion storage capabilities of the carbon additive, likely through their ordered and porous structures.

Conclusion

In conclusion, we report the first framework materials constructed from antiaromatic building blocks. We have developed three highly porous and crystalline COFs and two porous organic polymers (POPs) based on dibenzopentalene. The antiaromatic materials show broad optical absorption of up to 800 nm. **PhDBP-TFP** COF is semiconductive (4×10^{-8} S cm^{-1}) in the doped state and shows distinct photoconductivity in the range of 375–660 nm LED irradiation. Owing to their antiaromatic character, DBPs are stabilized in their oxidized and reduced state making them potential candidates for battery applications. Using crystalline **PhDBP-TFP** COF as the positive electrode-active material in a dual-ion Li-organic battery, a superior capacity of 26 mAh g^{-1} was found to that for amorphous **DBP-Ph-TFP** POP with 14 mAh g^{-1}. Compared to the structurally similar but aromatic **BND-TFP** COF, the DBP units in **PhDBP-TFP** COF enhanced the charge storage capabilities of the COF as positive electrode material. As negative electrode materials, both **PhDBP-TFP** COF and **DBP-Ph-TFP** POP showed reversible Li-ion storage and increased the specific capacities of the conductive carbon employed, likely due to their ordered and porous structure. Overall, this work demonstrates that antiaromaticity offers a new design principle for framework materials in energy storage applications.

Associated Content

CCDC 2082679, 2098056, and 2129185 contain the supplementary crystallographic data for this paper. The data can be obtained free of charge via www.ccdc.cam.ac.uk/data_request/cif, or by emailing data_request@ccdc.cam.ac.uk, or by contacting The Cambridge Crystallographic Data Centre, 12 Union Road, Cambridge CB2 1EZ, UK; fax: +44 1223 336033.

Author Information

Corresponding Authors

Birgit Esser – Institute for Organic Chemistry II and Advanced Materials, Ulm University, Albert-Einstein-Allee 11, 89081 Ulm, Germany; orcid.org/0000-0002-2430-1380; Email: birgit.esser@uni-ulm.de

Oliver Dumele – *Department of Chemistry & IRIS Adlershof, Humboldt University of Berlin, Berlin D-12489, Germany;* orcid.org/0000-0002-3277-6570; Email: oliver.dumele@hu-berlin.de

Authors

Josefine Sprachmann – *Department of Chemistry & IRIS Adlershof, Humboldt University of Berlin, Berlin 12489,* Germany

Tommy Wachsmuth – *Department of Chemistry & IRIS Adlershof, Humboldt University of Berlin, Berlin 12489,* Germany

Manik Bhosale – Institute for Organic Chemistry II and Advanced Materials, Ulm University, Albert-Einstein-Allee 11, 89081 Ulm, Germany

David Burmeister – *Department of Chemistry & IRIS Adlershof, Humboldt University of Berlin, Berlin 12489,* Germany

Glen Smales – *Bundesanstalt für Materialforschung und -prüfung (BAM), 12205 Berlin, Germany*

Zdravko Kochovski – *Department for Electrochemical Energy Storage, Helmholtz-Zentrum Berlin für Materialien und Energie, 14109 Berlin, Germany*

Niklas Grabicki – *Department of Chemistry & IRIS Adlershof, Humboldt University of Berlin, Berlin 12489,* Germany

Funding

This work was supported by the German Research Foundation for funding within the priority program SPP 2248 Polymer-Based Batteries (project number 441236036) and the German Federal Ministry of Education and Research (BMBF BattFutur, 03XP0457). O.D. thanks the FCI for a Liebig scholarship. This work contributes to the research performed at CELEST (Center for Electrochemical Energy Storage Ulm-Karlsruhe) and was funded by the German Research Foundation (DFG) under Project ID 390874152 (POLiS Cluster of Excellence, EXC 2154).

Notes

The authors declare no competing financial interest.

Acknowledgments

We thank Linos Madalo for scaling up the synthesis of the molecular building blocks, Dr. Jan Wössner for providing 5,10-diphenyl-DBP, Dr. Lutz Grubert for measuring solution phase cyclic voltammetry, Prof. Philipp Adelhelm for access to SEM, and Sebastian Pallasch for helpful discussions. O.D. is grateful to Stefan Hecht for his continuous support.

References

(1) Breslow, R. Antiaromaticity. *Acc. Chem. Res.* **1973**, *6*, 393–398.

(2) Minsky, A.; Meyer, A. Y.; Rabinovitz, M. Paratropicity and Antiaromaticity: Role of the HOMO–LUMO Energy Gap. *Tetrahedron* **1985**, *41*, 785–791.

(3) Gellini, C.; Salvi, P. R. Structures of Annulenes and Model Annulene Systems in the Ground and Lowest Excited States. *Symmetry.* **2010**, *2*, 1846–1924.

(4) Baird, N. C. Quantum Organic Photochemistry. II. Resonance and Aromaticity in the Lowest $^3\pi\pi^*$ State of Cyclic Hydrocarbons. *J. Am. Chem. Soc.* **1972**, *94*, 4941–4948.

(5) Ottosson, H. Exciting Excited-State Aromaticity. *Nat. Chem.* **2012**, *4*, 969–971.

(6) Kawase, T.; Fujiwara, T.; Kitamura, C.; Konishi, A.; Hirao, Y.; Matsumoto, K.; Kurata, H.; Kubo, T.; Shinamura, S.; Mori, H.; Miyazaki, E.; Takimiya, K. Dinaphthopentalenes: Pentalene Derivatives for Organic Thin-Film Transistors. *Angew. Chem. Int. Ed.* **2010**, *49*, 7728–7732.

(7) Chase, D. T.; Fix, A. G.; Kang, S. J.; Rose, B. D.; Weber, C. D.; Zhong, Y.; Zakharov, L. N.; Lonergan, M. C.; Nuckolls, C.; Haley, M. M. 6,12-Diarylindeno[1,2-*b*]fluorenes: Syntheses, Photophysics, and Ambipolar OFETs. *J. Am. Chem. Soc.* **2012**, *134*, 10349–10352.

(8) Shin, J. Y.; Yamada, T.; Yoshikawa, H.; Awaga, K.; Shinokubo, H. An Antiaromatic Electrode-Active Material Enabling High Capacity and Stable Performance of Rechargeable Batteries. *Angew. Chem. Int. Ed.* **2014**, *53*, 3096–3101.

(9) Usuba, J.; Hayakawa, M.; Yamaguchi, S.; Fukazawa, A. Dithieno[*a,e*]pentalenes: Highly Antiaromatic Yet Stable π-Electron Systems without Bulky Substituents. *Chem. Eur. J.* **2021**, *27*, 1638–1647.

(10) Cao, J.; London, G.; Dumele, O.; Von Wantoch Rekowski, M.; Trapp, N.; Ruhlmann, L.; Boudon, C.; Stanger, A.; Diederich, F. New Reactions of a Dibenzo[*a,e*]pentalene. *J. Am. Chem. Soc.* **2015**, *137*, 7178–7188.

(11) Strictly, aromaticity and antiaromaticity are concepts for monocyclic systems that can be extended to more complex polycyclic scaffolds, see refs. 12–14.

(12) Solà, M. Aromaticity Rules. *Nat. Chem.* **2022**, *14*, 585–590.

(13) Randic, M. Aromaticity of Polycyclic Conjugated Hydrocarbons. *Chem. Rev.* **2003**, *103*, 3449–3605.

(14) Warren, G. I.; Barker, J. E.; Zakharov, L. N.; Haley, M. M. Enhancing the Antiaromaticity of s-Indacene through Naphthothiophene Fusion. *Org. Lett* **2021**, *23*, 5012–5017.

(15) Konishi, A.; Yasuda, M. Breathing New Life into Nonalternant Hydrocarbon Chemistry: Syntheses and Properties of Polycyclic Hydrocarbons Containing Azulene, Pentalene, and Heptalene Frameworks. *Chem. Lett.* **2021**, *50*, 195–212.

(16) Grenz, D. C.; Schmidt, M.; Kratzert, D.; Esser, B. Dibenzo[*a,e*]pentalenes with Low-Lying LUMO Energy Levels as Potential n-Type Materials. *J. Org. Chem.* **2018**, *83*, 656–663.

(17) Oshima, H.; Fukazawa, A.; Yamaguchi, S. Facile Synthesis of Polycyclic Pentalenes with Enhanced Hückel Antiaromaticity. *Angew. Chem. Int. Ed.* **2017**, *56*, 3270–3274.

(18) Usuba, J.; Fukazawa, A. Thiophene-Fused 1,4-Diazapentalene: A Stable C=N-Containing π-Conjugated System with Restored Antiaromaticity. *Chem. Eur. J.* **2021**, *27*, 16127–16134.

(19) Yuan, B.; Zhuang, J.; Kirmess, K. M.; Bridgmohan, C. N.; Whalley, A. C.; Wang, L.; Plunkett, K. N. Pentaleno[1,2-*a*:4,5′]Diacenaphthylenes: Uniquely Stabilized Pentalene Derivatives. *J. Org. Chem.* **2016**, *81*, 8312–8318.

(20) Hafner, K. Pentalen - Die Lösung eines Alten Problems. *Nachr. Chem. Tech. Lab* **1980**, *28*, 222–226.

(21) Brand, K. Über Gefärbte Kohlenwasserstoffe der Diphensuccinden-Reihe. *Chem. Ber.* **1912**, *45*, 3071–3077.

(22) Hopf, H. Pentalenes - From Highly Reactive Antiaromatics to Substrates for Material Science. *Angew. Chem. Int. Ed.* **2013**, *52*, 12224–12226.

(23) Saito, M.; Nakamura, M.; Tajima, T. New Reactions of a Dibenzo[*a*,*e*]pentalene. *Chem. Eur. J.* **2008**, *14*, 6062–6068.

(24) Levi, Z. U.; Tilley, T. D. Versatile Synthesis of Pentalene Derivatives via the Pd-Catalyzed Homocoupling of Haloenynes. *J. Am. Chem. Soc.* **2009**, *131*, 2796–2797.

(25) Zhang, H.; Karasawa, T.; Yamada, H.; Wakamiya, A.; Yamaguchi, S. Intramolecular Reductive Double Cyclization of *o,o'*-Bis(Arylcarbonyl) Diphenylacetylenes: Synthesis of Ladder π-Conjugated Skeletons. *Org. Lett.* **2009**, *11*, 3076–3079.

(26) Wilbuer, J.; Grenz, D. C.; Schnakenburg, G.; Esser, B. Donor-and Acceptor-Functionalized Dibenzo[*a,e*]pentalenes: Modulation of the Electronic Band Gap. *Org. Chem. Front.* **2017**, *4*, 658–663.

(27) Kawase, T.; Nishida, J. I. π-Extended Pentalenes: The Revival of the Old Compound from New Standpoints. *Chem. Rec.* **2015**, *15*, 1045–1059.

(28) Yin, F.; Wang, L.; Yang, X.; Liu, M.; Geng, H.; Liao, Y.; Liao, Q.; Fu, H. High Performance Single-Crystalline Organic Field-Effect Transistors Based on Molecular-Modified Dibenzo[*a,e*]pentalenes Derivatives. *New J. Chem.* **2020**, *44*, 17552–17557.

(29) Hermann, M.; Wu, R.; Grenz, D. C.; Kratzert, D.; Li, H.; Esser, B. Thioether- and Sulfone-Functionalized Dibenzopentalenes as n-Channel Semiconductors for Organic Field-Effect Transistors. *J. Mater. Chem. C* **2018**, *6*, 5420–5426.

(30) Nakano, M.; Osaka, I.; Takimiya, K.; Koganezawa, T. Novel Dibenzo[*a,e*]pentalene-Based Conjugated Polymers. *J. Mater. Chem. C* **2013**, *2*, 64–70.

(31) Wu, Y.; Wang, Y.; Chen, J.; Zhang, G.; Yao, J.; Zhang, D.; Fu, H. Intramolecular Singlet

Fission in an Antiaromatic Polycyclic Hydrocarbon. *Angew. Chem. Int. Ed.* **2017**, *56*, 9400–9404.

(32) Wang, L.; Wu, Y.; Liu, Y.; Wang, L.; Yao, J.; Fu, H. Morphology Independent Triplet Formation in Pentalene Films: Singlet Fission as the Triplet Formation Mechanism. *J. Chem. Phys.* **2019**, *151*, 124701.

(33) Liu, Y.; Wu, Y.; Wang, L.; Wang, L.; Yao, J.; Fu, H. Efficient Triplet Pair Separation from Intramolecular Singlet Fission in Dibenzopentalene Derivatives. *Sci. China Chem.* **2019**, *62*, 1037–1043.

(34) Itamar, W.; Becker, J. Y.; Mordecai, R. Manifestation of Dual Aromaticity in Doubly Charged Annelated Pentalenes. *J. Am. Chem. Soc.* **1979**, *101*, 395–401.

(35) Hermann, M.; Böttcher, T.; Schorpp, M.; Richert, S.; Wassy, D.; Krossing, I.; Esser, B. Cations and Anions of Dibenzo[*a,e*]pentalene and Reduction of a Dibenzo[*a,e*]pentalenophane. *Chem. Eur. J.* **2021**, *27*, 4964–4970.

(36) Gannett, C. N.; Melecio-Zambrano, L.; Theibault, M. J.; Peterson, B. M.; Fors, B. P.; Abruña, H. D. Organic Electrode Materials for Fast-Rate, High-Power Battery Applications. *Mater. Reports Energy* **2021**, *1*, 100008.

(37) Esser, B.; Dolhem, F.; Becuwe, M.; Poizot, P.; Vlad, A.; Brandell, D. A Perspective on Organic Electrode Materials and Technologies for next Generation Batteries. *J. Power Sources* **2021**, *482*, 228814.

(38) Lu, Y.; Zhang, Q.; Li, L.; Niu, Z.; Chen, J. Design Strategies toward Enhancing the Performance of Organic Electrode Materials in Metal-Ion Batteries. *Chem* **2018**, *4*, 2786–2813.

(39) Diercks, C. S.; Yaghi, O. M. The Atom, the Molecule, and the Covalent Organic Framework. *Science* **2017**, *355*, 923.

(40) Huang, N.; Wang, P.; Jiang, D. Covalent Organic Frameworks: A Materials Platform for Structural and Functional Designs. *Nat. Rev. Mater.* **2016**, *1*, 16068.

(41) Sun, T.; Xie, J.; Guo, W.; Li, D. S.; Zhang, Q. Covalent–Organic Frameworks: Advanced Organic Electrode Materials for Rechargeable Batteries. *Adv. Energy Mater*. **2020**, *19*, 1904199.

(42) Zhou, L.; Jo, S.; Park, M.; Fang, L.; Zhang, K.; Fan, Y.; Hao, Z.; Kang, Y. M. Structural Engineering of Covalent Organic Frameworks for Rechargeable Batteries. *Adv. Energy Mater.* **2021**, *11*, 2003054.

(43) Zhu, D.; Xu, G.; Barnes, M.; Li, Y.; Tseng, C. P.; Zhang, Z.; Zhang, J. J.; Zhu, Y.; Khalil, S.; Rahman, M. M.; Verduzco, R.; Ajayan, P. M. Covalent Organic Frameworks for Batteries. *Adv. Funct. Mater.* **2021**, *31*, 2100505.

(44) Nguyen, H. L.; Gropp, C.; Hanikel, N.; Möckel, A.; Lund, A.; Yaghi, O. M. Hydrazine-Hydrazide-Linked Covalent Organic Frameworks for Water Harvesting. *ACS Cent. Sci.* **2022**, *42*, 18.

(45) Lyu, H.; Li, H.; Hanikel, N.; Wang, K.; Yaghi, O. M. Covalent Organic Frameworks for Carbon Dioxide Capture from Air. *J. Am. Chem. Soc.* **2022**, *144*, 12989–12995.

(46) Traxler, M.; Gisbertz, S.; Pachfule, P.; Schmidt, J.; Roeser, J.; Reischauer, S.; Rabeah, J.; Pieber, B.; Thomas, A. Acridine-Functionalized Covalent Organic Frameworks (COFs) as Photocatalysts for Metallaphotocatalytic C−N Cross-Coupling. *Angew. Chem. Int. Ed.* **2022**, *61*, e202117738.

(47) Yao, L.; Rodríguez-Camargo, A.; Xia, M.; Mücke, D.; Guntermann, R.; Liu, Y.; Grunenberg, L.; Jiménez-Solano, A.; Emmerling, S. T.; Duppel, V.; Sivula, K.; Bein, T.;

Qi, H.; Kaiser, U.; Grätzel, M.; Lotsch, B. V. Covalent Organic Framework Nanoplates Enable Solution-Processed Crystalline Nanofilms for Photoelectrochemical Hydrogen Evolution. *J. Am. Chem. Soc.* **2022**, *144*, 10291–10300.

(48) Pachfule, P.; Acharjya, A.; Roeser, J.; Langenhahn, T.; Schwarze, M.; Schomäcker, R.; Thomas, A.; Schmidt, J. Diacetylene Functionalized Covalent Organic Framework (COF) for Photocatalytic Hydrogen Generation. *J. Am. Chem. Soc.* **2018**, *140*, 1423–1427.

(49) Chen, W.; Wang, L.; Mo, D.; He, F.; Wen, Z.; Wu, X.; Xu, H.; Chen, L. Modulating Benzothiadiazole-Based Covalent Organic Frameworks via Halogenation for Enhanced Photocatalytic Water Splitting. *Angew. Chem. Int. Ed.* **2020**, *59*, 16902–16909.

(50) Wan, S.; Guo, J.; Kim, J.; Ihee, H.; Jiang, D. A Photoconductive Covalent Organic Framework: Self-Condensed Arene Cubes Composed of Eclipsed 2D Polypyrene Sheets for Photocurrent Generation. *Angew. Chem. Int. Ed.* **2009**, *48*, 5439–5442.

(51) Bessinger, D.; Muggli, K.; Beetz, M.; Auras, F.; Bein, T. Fast-Switching Vis-IR Electrochromic Covalent Organic Frameworks. *J. Am. Chem. Soc.* **2021**, *143*, 7351–7357.

(52) Ascherl, L.; Evans, E. W.; Gorman, J.; Orsborne, S.; Bessinger, D.; Bein, T.; Friend, R. H.; Auras, F. Perylene-Based Covalent Organic Frameworks for Acid Vapor Sensing. *J. Am. Chem. Soc.* **2019**, *141*, 15693–15699.

(53) Ghosh, S.; Tsutsui, Y.; Kawaguchi, T.; Matsuda, W.; Nagano, S.; Suzuki, K.; Kaji, H.; Seki, S. Band-like Transport of Charge Carriers in Oriented Two-Dimensional Conjugated Covalent Organic Frameworks. *Chem. Mater.* **2022**, *34*, 736–745.

(54) Lakshmi, V.; Liu, C.-H.; Rao, R.; Chen, Y.; Fang, Y.; Dadvand, A.; Hamzehpoor, E.; Sakai-Otsuka, Y.; Stein, R. S.; Perepichka, D. F. A Two-Dimensional Poly(Azatriangulene) Covalent Organic Framework with Semiconducting and Paramagnetic States. *J. Am. Chem. Soc.* **2020**, *142*, 2155–2160.

(55) Meng, Z.; Stolz, R. M.; Mirica, K. A. Two-Dimensional Chemiresistive Covalent Organic Framework with High Intrinsic Conductivity. *J. Am. Chem. Soc.* **2019**, *141*, 11929–11937.

(56) Keller, N.; Bein, T. Optoelectronic Processes in Covalent Organic Frameworks. *Chem. Soc. Rev.* **2021**, *50*, 1813–1845.

(57) Meng, Z.; Aykanat, A.; Mirica, K. A. Proton Conduction in 2D Aza-Fused Covalent Organic Frameworks. *Chem. Mater.* **2019**, *31*, 819–825.

(58) Biswal, B. P.; Valligatla, S.; Wang, M.; Banerjee, T.; Saad, N. A.; Mariserla, B. M. K.; Chandrasekhar, N.; Becker, D.; Addicoat, M.; Senkovska, I.; Berger, R.; Rao, D. N.; Kaskel, S.; Feng, X. Nonlinear Optical Switching in Regioregular Porphyrin Covalent Organic Frameworks. *Angew. Chem. Int. Ed.* **2019**, *131*, 6970–6974.

(59) Byun, Y.; Xie, L. S.; Fritz, P.; Ashirov, T.; Dincă, M.; Coskun, A. A Three-Dimensional Porous Organic Semiconductor Based on Fully sp^2-Hybridized Graphitic Polymer. *Angew. Chem. Int. Ed.* **2020**, *59*, 15166–15170.

(60) Arab, P.; Rabbani, M. G.; Sekizkardes, A. K.; Islamoğlu, T.; El-Kaderi, H. M. Copper(I)-Catalyzed Synthesis of Nanoporous Azo-Linked Polymers: Impact of Textural Properties on Gas Storage and Selective Carbon Dioxide Capture. *Chem. Mater.* **2014**, *26*, 1385–1392.

(61) Gu, C.; Huang, N.; Chen, Y.; Qin, L.; Xu, H.; Zhang, S.; Li, F.; Ma, Y.; Jiang, D. π-Conjugated Microporous Polymer Films: Designed Synthesis, Conducting Properties, and Photoenergy Conversions. *Angew. Chem. Int. Ed.* **2015**, *54*, 13594–13598.

(62) Evans, A. M.; Strauss, M. J.; Corcos, A. R.; Hirani, Z.; Ji, W.; Hamachi, L. S.; Aguilar-Enriquez, X.; Chavez, A. D.; Smith, B. J.; Dichtel, W. R. Two-Dimensional Polymers and Polymerizations. *Chem. Rev*. **2022**, *122*, 442–564.

(63) Gao, H.; Neale, A. R.; Zhu, Q.; Bahri, M.; Wang, X.; Yang, H.; Xu, Y.; Clowes, R.; Browning, N. D.; Little, M. A.; Hardwick, L. J.; Cooper, A. I. A Pyrene-4,5,9,10-tetraone-Based Covalent Organic Framework Delivers High Specific Capacity as a Li-Ion Positive Electrode. *J. Am. Chem. Soc.* **2022**, *144*, 9434–9442.

(64) Vitaku, E.; Gannett, C. N.; Carpenter, K. L.; Shen, L.; Abruña, H. D.; Dichtel, W. R. Phenazine-Based Covalent Organic Framework Cathode Materials with High Energy and Power Densities. *J. Am. Chem. Soc.* **2020**, *142*, 16–20.

(65) Wang, G.; Chandrasekhar, N.; Biswal, B. P.; Becker, D.; Paasch, S.; Brunner, E.; Addicoat, M.; Yu, M.; Berger, R.; Feng, X. A Crystalline, 2D Polyarylimide Cathode for Ultrastable and Ultrafast Li Storage. *Adv. Mater.* **2019**, *31*, 1901478.

(66) Xu, F.; Jin, S.; Zhong, H.; Wu, D.; Yang, X.; Chen, X.; Wei, H.; Fu, R.; Jiang, D. Electrochemically Active, Crystalline, Mesoporous Covalent Organic Frameworks on Carbon Nanotubes for Synergistic Lithium-Ion Battery Energy Storage. *Sci. Rep.* **2015**, *5*, 8225.

(67) Gao, H.; Zhu, Q.; Neale, A. R.; Bahri, M.; Wang, X.; Yang, H.; Liu, L.; Clowes, R.; Browning, N. D.; Sprick, R. S.; Little, M. A.; Hardwick, L. J.; Cooper, A. I. Integrated Covalent Organic Framework/Carbon Nanotube Composite as Li-Ion Positive Electrode with Ultra-High Rate Performance. *Adv. Energy Mater.* **2021**, *11*, 2101880.

(68) Lei, Z.; Yang, Q.; Xu, Y.; Guo, S.; Sun, W.; Liu, H.; Lv, L. P.; Zhang, Y.; Wang, Y. Boosting Lithium Storage in Covalent Organic Framework via Activation of 14-Electron Redox Chemistry. *Nat. Commun.* **2018**, *9*, 576.

(69) Haldar, S.; Wang, M.; Bhauriyal, P.; Hazra, A.; Khan, A. H.; Bon, V.; Isaacs, M. A.; De, A.; Shupletsov, L.; Boenke, T.; Grothe, J.; Heine, T.; Brunner, E.; Feng, X.; Dong, R.; Schneemann, A.; Kaskel, S. Porous Dithiine-Linked Covalent Organic Framework as a Dynamic Platform for Covalent Polysulfide Anchoring in Lithium-Sulfur Battery Cathodes. *J. Am. Chem. Soc.* **2022**, *144*, 9101–9112.

(70) Sun, T.; Xie, J.; Guo, W.; Li, D. S.; Zhang, Q. Covalent–Organic Frameworks: Advanced Organic Electrode Materials for Rechargeable Batteries. *Adv. Energy Mater.* **2020**, *10*, 1904199.

(71) Lee, S.; Kwon, G.; Ku, K.; Yoon, K.; Jung, S. K.; Lim, H. D.; Kang, K. Recent Progress in Organic Electrodes for Li and Na Rechargeable Batteries. *Adv. Mater.* **2018**, *30*, 1704682.

(72) Li, X.; Yang, J. Realizing Two-Dimensional Magnetic Semiconductors with Enhanced Curie Temperature by Antiaromatic Ring Based Organometallic Frameworks. *J. Am. Chem. Soc.* **2019**, *141*, 109–112.

(73) Corminboeuf, C.; Schleyer, P. v. R.; Warner, P. Are Antiaromatic Rings Stacked Face-to-Face Aromatic? *Org. Lett.* **2007**, *9*, 3263–3266.

(74) Nozawa, R.; Kim, J.; Oh, J.; Lamping, A.; Wang, Y.; Shimizu, S.; Hisaki, I.; Kowalczyk, T.; Fliegl, H.; Kim, D.; Shinokubo, H. Three-Dimensional Aromaticity in an Antiaromatic Cyclophane. *Nat. Commun.* **2019**, *10*, 3576.

(75) Kawashima, H.; Ukai, S.; Nozawa, R.; Fukui, N.; Fitzsimmons, G.; Kowalczyk, T.; Fliegl, H.; Shinokubo, H. Determinant Factors of Three-Dimensional Aromaticity in Antiaromatic Cyclophanes. *J. Am. Chem. Soc.* **2021**, *143*, 10676–10685.

(76) Stanger, A. Nucleus-Independent Chemical Shifts (NICS): Distance Dependence and

Revised Criteria for Aromaticity and Antiaromaticity. *J. Org. Chem.* **2006**, *71*, 883–893.

(77) Kawase, T.; Konishi, A.; Hirao, Y.; Matsumoto, K.; Kurata, H.; Kubo, T. An Extremely Simple Dibenzopentalene Synthesis from 2-Bromo-1-ethynylbenzenes Using Nickel(0) Complexes: Construction of Its Derivatives with Various Functionalities. *Chem. Eur. J.* **2009**, *15*, 2653–2661.

(78) Xu, F.; Peng, L.; Orita, A.; Otera, J. Dihalo-Substituted Dibenzopentalenes: Their Practical Synthesis and Transformation to Dibenzopentalene Derivatives. *Org. Lett.* **2012**, *14*, 3970–3973.

(79) Nakano, M.; Osaka, I.; Takimiya, K.; Koganezawa, T. Novel Dibenzo[*a,e*]pentalene-Based Conjugated Polymers. *J. Mater. Chem. C* **2014**, *2*, 64–70.

(80) Wössner, J. S.; Wassy, D.; Weber, A.; Bovenkerk, M.; Hermann, M.; Schmidt, M.; Esser, B. Cyclodibenzopentalenes as Antiaromatic Curved Nanocarbons with High Strain and Strong Fullerene Binding. *J. Am. Chem. Soc.* **2021**, *143*, 12244–12252.

(81) Wössner, J. S.; Kohn, J.; Wassy, D.; Hermann, M.; Grimme, S.; Esser, B. Increased Antiaromaticity through Pentalene Connection in [*n*]Cyclo-1,5-dibenzopentalenes. *Org. Lett.* **2022**, *24*, 983–988.

(82) Wolfe, J. P.; Ahman, J.; Joseph, S.; Robert, S.; Buchwald Stephen. An Ammonia Equivalent for the Palladium-Catalyzed Amination of Aryl Halides and Triflates. *Tetrahedron Lett.* **1997**, *38*, 6367–6370.

(83) Vitaku, E.; Dichtel, W. R. Synthesis of 2D Imine-Linked Covalent Organic Frameworks through Formal Transimination Reactions. *J. Am. Chem. Soc.* **2017**, *139*, 12911–12914.

(84) Hermann, M.; Wassy, D.; Kratzert, D.; Esser, B. Dibenzo[*a,e*]pentalenophanes: Bending a Non-Alternant Hydrocarbon. *Chem. Eur. J.* **2018**, *24*, 7374–7387.

(85) BIOVIA, Dassault Systèmes. Materials Studio: San Diego **2022**.

(86) Sing, K. S. W.; Everett, D. H.; Haul, R. A. W.; Moscou, L.; Pierotti, R. A.; Rouquèrol, J.; Siemieniewska, T. Reporting Physisorption Data for Gas/Solid Systems with Special Reference to the Determination of Surface Area and Porosity. *Pure Appl. Chem.* **1985**, *57*, 603–619.

(87) Kandambeth, S.; Mallick, A.; Lukose, B.; Mane, M. V; Heine, T.; Banerjee, R. Construction of Crystalline 2D Covalent Organic Frameworks with Remarkable Chemical (Acid/Base) Stability via a Combined Reversible and Irreversible Route. *J. Am. Chem. Soc.* **2012**, *134*, 19524–19527.

(88) Burke, D. W.; Sun, C.; Castano, I.; Flanders, N. C.; Evans, A. M.; Vitaku, E.; McLeod, D. C.; Lambeth, R. H.; Chen, L. X.; Gianneschi, N. C.; Dichtel, W. R. Acid Exfoliation of Imine-Linked Covalent Organic Frameworks Enables Solution Processing into Crystalline Thin Films. *Angew. Chem. Int. Ed.* **2020**, *59*, 5165–5171.

(89) Eder, S.; Yoo, D. J.; Nogala, W.; Pletzer, M.; Santana Bonilla, A.; White, A. J. P.; Jelfs, K. E.; Heeney, M.; Choi, J. W.; Glöcklhofer, F. Switching between Local and Global Aromaticity in a Conjugated Macrocycle for High-Performance Organic Sodium-Ion Battery Anodes. *Angew. Chem. Int. Ed.* **2020**, *59*, 12958–12964.

(90) Laoire, C. O.; Plichta, E.; Hendrickson, M.; Mukerjee, S.; Abraham, K. M. Electrochemical Studies of Ferrocene in a Lithium Ion Conducting Organic Carbonate Electrolyte. *Electrochim. Acta* **2009**, *54*, 6560–6564.

(91) Singh, V.; Kim, J.; Kang, B.; Moon, J.; Kim, S.; Kim, W. Y.; Byon, H. R. Thiazole-Linked Covalent Organic Framework Promoting Fast Two-Electron Transfer for Lithium-Organic Batteries. *Adv. Energy Mater.* **2021**, *11*, 2003735.

(92) Wang, Z.; Li, Y.; Liu, P.; Qi, Q.; Zhang, F.; Lu, G.; Zhao, X.; Huang, X. Few Layer Covalent Organic Frameworks with Graphene Sheets as Cathode Materials for Lithium-Ion Batteries. *Nanoscale* **2019**, *11*, 5330–5335.

(93) Biswal, B. P.; Chandra, S.; Kandambeth, S.; Lukose, B.; Heine, T.; Banerjee, R. Mechanochemical Synthesis of Chemically Stable Isoreticular Covalent Organic Frameworks. *J. Am. Chem. Soc.* **2013**, *135*, 5328–5331.

(94) Ma, Q.; Zheng, J.; Kang, H.; Zhang, L.; Zhang, Q.; Li, H.; Wang, R.; Zhou, T.; Chen, Q.; Liu, A.; Li, H.; Zhang, C. Conjugated Porous Polydiaminophenylsulfone-Triazine Polymer — A High-Performance Anode for Li-Ion Batteries. *ACS Appl. Mater. Interfaces* **2021**, *13*, 43002–43010.

(95) Shen, J.; Yuan, D.; Qiao, Y.; Shen, X.; Zhang, Z.; Zhong, Y.; Yi, Y.; Zhu, X. Diaceno[a,e]Pentalenes from Homoannulations of *o*-Alkynylaryliodides Utilizing a Unique $Pd(OAc)_2$ n-Bu_4NOAc Catalytic Combination. *Org. Lett.* **2014**, *16*, 4924–4927.